Scalable robust photothermal superhydrophobic coatings for efficient anti-icing and de-icing in simulated/real environments

Mingyuan Mao [1,3], Jinfei Wei [1,3], Bucheng Li [1], Lingxiao Li [1,2], Xiaopeng Huang [1] & Junping Zhang [1,2] ✉

Photothermal superhydrophobic coatings are supposed promising to prevent ice accumulation on infrastructures but often experience significant performance degradation in real icing conditions and lack mechanical robustness. Here, we report design of robust photothermal superhydrophobic coatings with three-tier hierarchical micro-/nano-/nanostructures by deposition of nanosized MOFs on natural attapulgite nanorods, fluorination, controlled phase separation of a hydrophobic adhesive and spraying assembly. Phase separation degree and adhesive content significantly influence the coatings' properties by regulating the structural parameters and morphology. In simulated/real icing environments, the coatings simultaneously show (i) high superhydrophobicity and stable Cassie-Baxter states due to their low-surface-energy, three-tier micro-/nano-/nanostructure, (ii) excellent photothermal effect primarily due to nanosized MOFs, and (iii) good mechanical robustness by the phase-separated adhesive, reinforcement with attapulgite and the coatings' self-similar structure. Accordingly, combined with low thermal conductivity, the coatings exhibit remarkable anti-icing/frosting (e.g., no freezing in at least 150 min and almost free of frost in 25 min) and de-icing/frosting performances (e.g., fast de-icing in 12.7 min and fast de-frosting in 16.7 min) in such environments. Furthermore, we realize large-scale preparation of the coatings at reasonable costs. The coatings have great application potential for anti-icing and de-icing in the real world by efficiently using natural sunlight.

Icing is a beautiful natural phenomenon in cold weather, but it poses a serious threat to the safety and reliability of various infrastructures, such as power grids, wind turbine blades, and bridges[1–3]. This can lead to substantial economic losses and even casualties (Supplementary Table 1). To address this issue, various active de-icing methods including manual, mechanical, thermal, laser, electromagnetic, and ultrasonic de-icing have been proposed[4]. However, these methods are often inefficient, time-consuming, and/or energy-intensive[5]. In recent years, some passive anti-icing strategies like superhydrophobic (SH) coatings[6], slippery liquid-infused porous surfaces[7,8], anti-freeze proteins[9,10], and gel materials[11,12] have received great attention due to their advantages

[1]Center of Resource Chemistry and Energy Materials, Key Laboratory of Clay Mineral of Gansu Province, and State Key Laboratory of Solid Lubrication, Lanzhou Institute of Chemical Physics, Chinese Academy of Sciences, Lanzhou, PR China. [2]Center of Materials Science and Optoelectronics Engineering, University of Chinese Academy of Sciences, Beijing, PR China. [3]These authors contributed equally: Mingyuan Mao, Jinfei Wei. ✉e-mail: jpzhang@licp.cas.cn

of high efficiency, convenience, low cost and zero energy input, etc.

SH coatings have become one of the most promising passive anti-icing strategies, as they can effectively delay ice formation and reduce ice adhesion strength due to their high contact angle (CA), low sliding angle (SA), and consequently, reduced solid-liquid contact area[3,13]. So far, SH anti-icing coatings have become an important sub-field of SH coatings[14]. Great progress has been made in their preparation[3,15], theory[1,16] and practical applications[17], etc. Nevertheless, SH coatings can only delay ice formation but cannot prevent it entirely[18]. Once icing occurs on SH coatings, de-icing remains challenging, similar to conventional coatings[13].

Therefore, photothermal SH coatings with both passive anti-icing and active de-icing functions are emerging as a very effective and sustainable anti-icing/de-icing protocol[19-21]. The photothermal effect can increase surface temperature of SH coatings by converting solar energy into heat, and thus further postpone or even inhibit icing and accelerate de-icing[22]. When the outdoor temperature is slightly below zero, the surface temperature of photothermal SH coatings may be above zero[23] and thus icing can be completely inhibited[24]. Up to now, various photothermal materials like Mxene[25], Fe_3O_4[26], TiN[5], graphene[27], carbon nanotubes[28], carbon black[29], and MOFs[30] have been integrated into SH coatings for passive anti-icing and active de-icing. Although great progress has been achieved in developing photothermal SH coatings[31-33], there are some key issues hindering their practical applications. (i) Good anti-icing performances have been reported for many SH coatings, but the anti-icing tests were often performed by placing the coatings on cold plates in high ambient temperature (≥ 0 °C) and low relative humidity (RH $\leq 60\%$) environments, which are far from the actual icing environments with low ambient temperature and high RH[17,34,35]. However, in actual icing environments, the anti-icing performance of SH coatings will degrade or even lose, due to decline of superhydrophobicity by condensation of supercooled water in their surface structure. (ii) The photothermal anti-icing and de-icing performances were often evaluated under high solar flux of $1\,kW\,m^{-2}$ (1 sun) and good results were obtained[32,36,37]. However, such high solar flux is impossible in real cold weather (Supplementary Table 2). Also, icing, anti-icing, and de-icing are the competitive results of ice nucleation/propagation, ice nucleation inhibition, and the photothermal SH effect[32]. Thus, it is essential to evaluate and optimize the photothermal anti-icing and de-icing performances in low ambient temperature, high RH, and weak solar flux environments. (iii) Poor mechanical robustness seriously inhibits applications of SH coatings in various fields including anti-icing and de-icing[38]. Thus, great efforts have been made to enhance the mechanical robustness and various strategies including micro-skeleton protection[17,39,40], self-healing[41,42], self-similar structures[43,44] and adhesives[45-49] have been invented, but scalable and low-cost methods remain to be developed. The self-similar structure means the surface and the interior share the same structure and chemical composition. When the surface is damaged, the exposed new surface is identical to the original[17,50]. The use of adhesives often causes great increase in surface energy of SH coatings. Non-solvent-induced phase separation of adhesives can form adhesive microparticles with low-surface-energy nanoparticles wrapping on them, thereby minimizing the impact of adhesives on the coatings' surface energy[17,50]. In a word, it is essential but great challenging to solve the above three issues simultaneously in order to move photothermal SH coatings to real-world applications.

Here, we report design and preparation of scalable robust photothermal SH coatings for passive anti-icing/frosting and active de-icing/frosting in low ambient temperature, high RH, and weak solar flux environments from the perspective of sustainable development. The coatings are fabricated via spraying a uniform suspension of micro-aggregates composed of fluorinated MOFs@attapulgite (ATP) nanorods and a silicone-modified polyester (SiP) adhesive onto substrates. The coatings show excellent superhydrophobicity, photothermal effect, and durability as well as exceptional passive anti-icing/frosting and active de-icing/defrosting performances in such simulated and real environments. Moreover, large-scale preparation of the photothermal SH coatings is realized.

Results and discussion

Design of robust photothermal SH coatings

Freezing of water droplets on a solid surface is closely related to ice nucleation[51]. According to the classical nucleation theory, at low temperature, there is a correlation between the nucleation Gibbs free energy barrier (ΔG) and the CA (θ) of the water droplet[51].

$$\Delta G = \pi \sigma_{lv} r^2 (2 - 3\cos\theta + \cos^3\theta)/3 \qquad (1)$$

where σ_{lv} is the liquid-vapor surface energy and r is the critical radius. So, the larger the θ when $\theta > 90°$, the higher the ΔG is and thus the better the anti-icing performance is.

In addition, the freezing process of water droplets on a solid surface follows the principle of energy conservation[52].

$$W_d + m_w L + Q_{exo} = (q_{wa} + q_r + \Phi)t \qquad (2)$$

where W_d is the kinetic energy of the droplet hitting the surface, m_w is the mass of the droplet, L is the latent heat of water, Q_{exo} is the heat released by water in the freezing process, q_{wa} is the natural convective heat transfer between the droplet's contact surface and the surroundings, q_r is the radiative heat transfer between the droplet's surface and the surroundings, Φ is the heat transfer between the droplet and the surface, and t is the droplet's freezing time. t and Φ are negative correlations. Φ and R are negative correlation according to formula (3)[52]:

$$\Phi = (T_w - T_a)/R \qquad (3)$$

where T_w is the internal temperature of the droplet as it freezes, T_a is the ambient temperature, and R is the thermal resistance of the droplet to the surface. R and λ_s are negative correlation according to formula (4)[52]:

$$R = (h - hX_i)/(2S_{ws}\lambda_s) + (hX_i)/(2S_{ws}\lambda_i) \qquad (4)$$

where λ_s is the thermal conductivity of the surface, λ_i is the thermal conductivity of ice, X_i is the influence factor of the thermal conductivity of ice, and h is the heat transfer coefficient between the water droplet and the surface. So, the smaller the λ_s of the surface, the greater the t is.

Furthermore, the interfacial heat transfer between the water droplet and the surface follows formula (5)[23]:

$$t_f = \rho L V / HS(T_m - T_s) \qquad (5)$$

where t_f is the duration from the water droplet begins phase transition to the solid ice droplet is completely formed, ρ is water density, V is volume of the water droplet, H is heat transfer coefficient, S is the contact area between the water droplet and the surface, T_m is equilibrium freezing temperature, and T_s is temperature of the surface. t_f and S are negative correlations. Therefore, the smaller the S, the greater the t_f is. Unfortunately, water droplets tend to transform from the Cassie-Baxter state to the Wenzel state on SH surfaces in low ambient temperature and high RH environments, resulting in greater S. So, a stable Cassie-Baxter state in such environments is essential for effective anti-icing.

According to the above theoretical analysis, SH surfaces with high water CA, low thermal conductivity, and stable Cassie-Baxter state in

low temperature and high RH environments should have good passive anti-icing performance. Introducing hierarchical porous structure can (i) enhance water CA of hydrophobic coatings[53,54], (ii) further reduce thermal conductivity of thermal insulating coatings[55], and (iii) improve stability of the Cassie-Baxter state on SH surfaces in low temperature and high RH environments[5]. Therefore, we designed the photothermal SH coatings with three-tier hierarchical micro-/nano-/nanostructures by deposition of nanosized photothermal MOFs on ATP nanorods, fluorination of MOFs@ATP, mixing F-MOFs@ATP with the SiP adhesive, phase separation of the adhesive, and finally spraying layer-by-layer assembly (Fig. 1). ATP is a kind of natural clay mineral with low thermal conductivity ($0.16\,W\,m^{-1}\,K^{-1}$) and high aspect ratio[56], which helps with forming reentrant structures[57,58]. SH coatings with such surface structure and chemical composition will have not only high CA and low thermal conductivity, but also a stable Cassie-Baxter state in low temperature and high RH environments, and thus good passive anti-icing performance.

To enhance the photothermal anti-icing and de-icing performances in low ambient temperature, high RH, and weak solar flux environments, we designed the photothermal SH coatings using the nanosized MOFs with high photothermal conversion efficiency[30]. Also, the hierarchical micro-/nano-/nanostructures can form numerous light traps in the SH coatings (Fig. 1), which will further enhance sunlight absorption by lengthening the optical path and decreasing reflection via multiple scattering of the incident light[59].

To achieve excellent mechanical robustness, we designed the photothermal SH coatings using a hydrophobic (CA = 85–90°) SiP adhesive with high hardness (1-2H) and a thermal conductivity of $0.29\,W\,m^{-1}\,K^{-1}$. The adhesive can enhance the coating's binding to the substrate and binding among the F-MOFs@ATP nanorods in the coating[46]. Furthermore, phase separation of the adhesive will cause the F-MOFs@ATP nanorods to encapsulate adhesive microparticles without compromising superhydrophobicity, unlike the traditional use of adhesives[50]. Also, we constructed the SH coatings with self-similar micro-/nano-/nanostructures by phase-separation the adhesive and spray-coating.

Preparation of SiP/F-MOFs@ATP coatings

In light of the aforementioned design principles, we prepared the robust photothermal SH SiP/F-MOFs@ATP coatings (Fig. 1). First, the nanosized photothermal MOFs were grown on the ATP nanorods via the reaction between $Cu(NO_3)_2$ and 2,3,6,7,10,11-hexahydroxy-triphenylene hydrate (HHTP). Numerous MOFs nanoparticles were formed on the ATP nanorods 30-40 nm in diameter and 600-800 nm in length, forming a two-tier nano-/nanostructure (Fig. 2a, b). Next, semi-solid F-MOFs@ATP nanorods with absorbed ethanol were produced by hydrolytic condensation of *1H,1H,2H,2H*-perfluorodecyltriethoxysilane (PFDTES), and tetraethoxysilane (TEOS) onto MOFs@ATP in ethanol followed by centrifugation. The MOFs@ATP nanorods were connected by perfluorodecyl polysiloxane (PF-POS, Fig. 2c). Subsequently, the semi-solid F-MOFs@ATP nanorods and additional ethanol were added successively into the SiP adhesive solution in dimethyl carbonate under vigorous stirring, during which ethanol as a non-solvent induced phase separation of the adhesive. As a result, the adhesion effect of the adhesive formed the micro-aggregates composed of the adhesive microparticles and the F-MOFs@ATP nanorods (Fig. 2d and Supplementary Fig. 1). The C, F, O, Si and Cu elements were detected in the SiP/F-MOFs@ATP micro-aggregates (Supplementary Fig. 2). The ethanol content controls the degree of phase separation. Lastly, the SiP/F-MOFs@ATP coatings were made by spray-coating the substrates with the homogeneous SiP/F-MOFs@ATP suspension and allowing them to cure at room temperature for 24 h (Supplementary Figs. 3 and 4).

The SiP/F-MOFs@ATP coating is highly microporous with a two-tier micro-/nanostructure made up of phase-separated SiP adhesive

microparticles (microstructure) with numerous F-MOFs@ATP nanorods (primary nanostructure) wrapped on them (Fig. 2e, f). At higher magnification, the coating shows a two-tier nano-/nanostructure with numerous MOFs (secondary nanostructure) on the tightly packed F-MOFs@ATP nanorods (Fig. 2g). Thus, we have successfully prepared the SiP/F-MOFs@ATP coating with a unique three-tier hierarchical micro-/nano-/nanostructure (surface roughness = 1.83 μm, Fig. 2i and Supplementary Table 3) by adhering to the design concepts outlined in the previous section. The coating also has a self-similar structure from top to bottom (Fig. 2h), which is helpful to enhance its mechanical robustness[50].

The surface chemical composition of the SiP/F-MOFs@ATP coating was examined by elemental mapping and XPS. The C, F, O, Si, and Cu elemental maps show that the surface and cross-section of the coating are chemically uniform (Supplementary Fig. 5). On the XPS spectra (Fig. 2j, k), the C 1s, O 1s, F 1s, and Si 2p peaks also appear but the Cu peak of MOFs is absent, because PF-POS covers MOFs@ATP and XPS has a very shallow detection depth of only a few nanometers[60]. This is confirmed by EDS elemental maps of MOFs@ATP with a strong Cu signal (Supplementary Fig. 6). The C 1s peak is assigned to C-C/(C-H), C-Si, O-C = O, CF_2 and CF_3[50,61,62]. The Si 2p peak is assigned to Si-OH, Si-O-Si and Si-C[61,62], and the F 1s peak is assigned to CF_2 and CF_3[63] (Supplementary Fig. 7). The C/F/O/Si ratio is 2.6/7.4/1.5/1 and the F content is up to 59% (Supplementary Table 4), indicating plentiful perfluorodecyl groups on the coating's surface to lower the surface energy[54].

The superhydrophobicity, mechanical robustness, and passive anti-icing performance of the SiP/F-MOFs@ATP coatings were systematically optimized and balanced by adjusting the ethanol content in the solvent of the SiP/F-MOFs@ATP suspension and the SiP adhesive content in the SiP/F-MOFs@ATP composites (Supplementary Figs. 8–13). These two parameters determine surface structure, chemical composition, and various performances of the coatings. Note that such optimization and balance were seldom in earlier research[17], but crucial for obtaining high-performance SH anti-icing coatings.

As the ethanol content increases from 22.4 wt% to 28.4 wt%, the coating's surface roughness rises from 1.44 μm to 1.83 μm, and the porosity increases from 35.87% to 68.54% (Supplementary Figs. 8 and 9). Further increases in ethanol content result in gradual decreases in both surface roughness and porosity. Additionally, the secondary nanostructure gradually appears with increasing the ethanol content. These changes are due to the enhanced phase separation of the SiP adhesive with higher ethanol contents. However, due to the very low surface energy of the coatings, superhydrophobicity exhibits only minor variations when tested with water, which has a high surface tension of $72.8\,mN\,m^{-1}$ (Supplementary Fig. 10a). The mechanical robustness and passive anti-icing performance, i.e., the water freezing time, are gradually enhanced to the best at 28.4 wt% ethanol content, and then decline with further increasing the ethanol content (Supplementary Fig. 10b and c). The improved passive anti-icing performance is primarily due to the increased porosity resulting from raising the ethanol content to 28.4 wt%. This increase in porosity reduces the coating's thermal conductivity to $0.19\,W\,m^{-1}\,K^{-1}$ (Supplementary Fig. 10d), thereby inhibiting heat transfer. Additionally, increasing the ethanol content to 28.4 wt% slightly enhances superhydrophobicity, which reduces the contact area between the coating and water. This, in turn, increases ΔG according to the classical nucleation theory[51], further hindering heat transfer. However, the anti-icing performance deteriorates with further increases in ethanol content due to the rise in thermal conductivity, even though superhydrophobicity remains relatively unchanged.

On the other hand, with an increase in the SiP adhesive content from 2.5 wt% to 12.5 wt%, the coatings' surface roughness decreases from 2.49 μm to 1.57 μm, the porosity decreases from 64.13% to 36.25%, the secondary nanostructure disappears (Supplementary
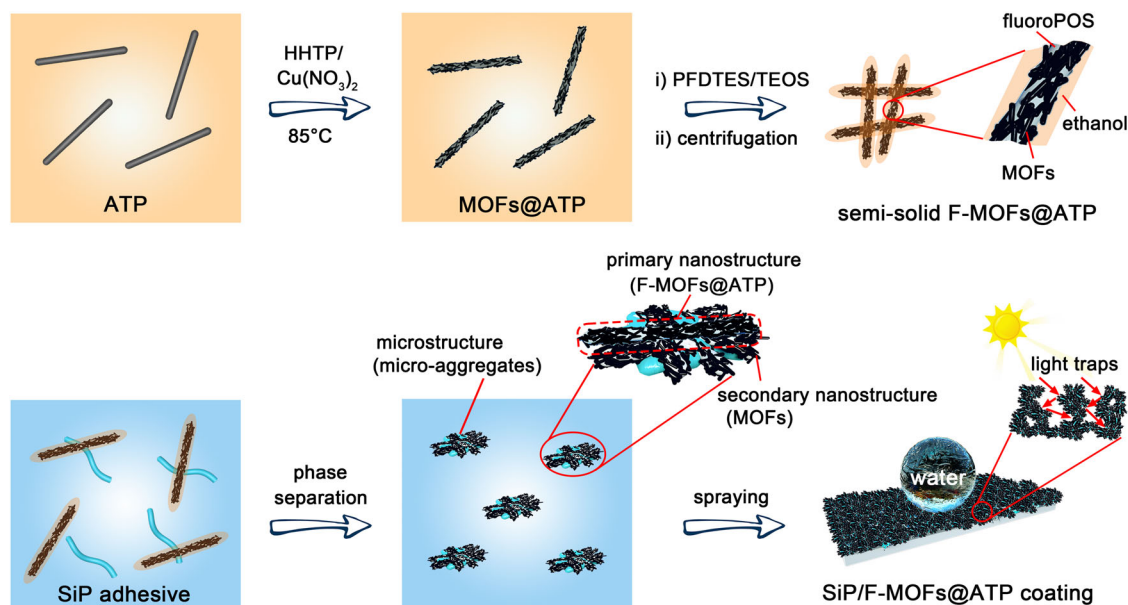
Fig. 1 | Schematic preparation of the robust photothermal SH SiP/F-MOFs@ATP coatings. Preparation of F-MOFs@ATP and the SiP/F-MOFs@ATP coatings.
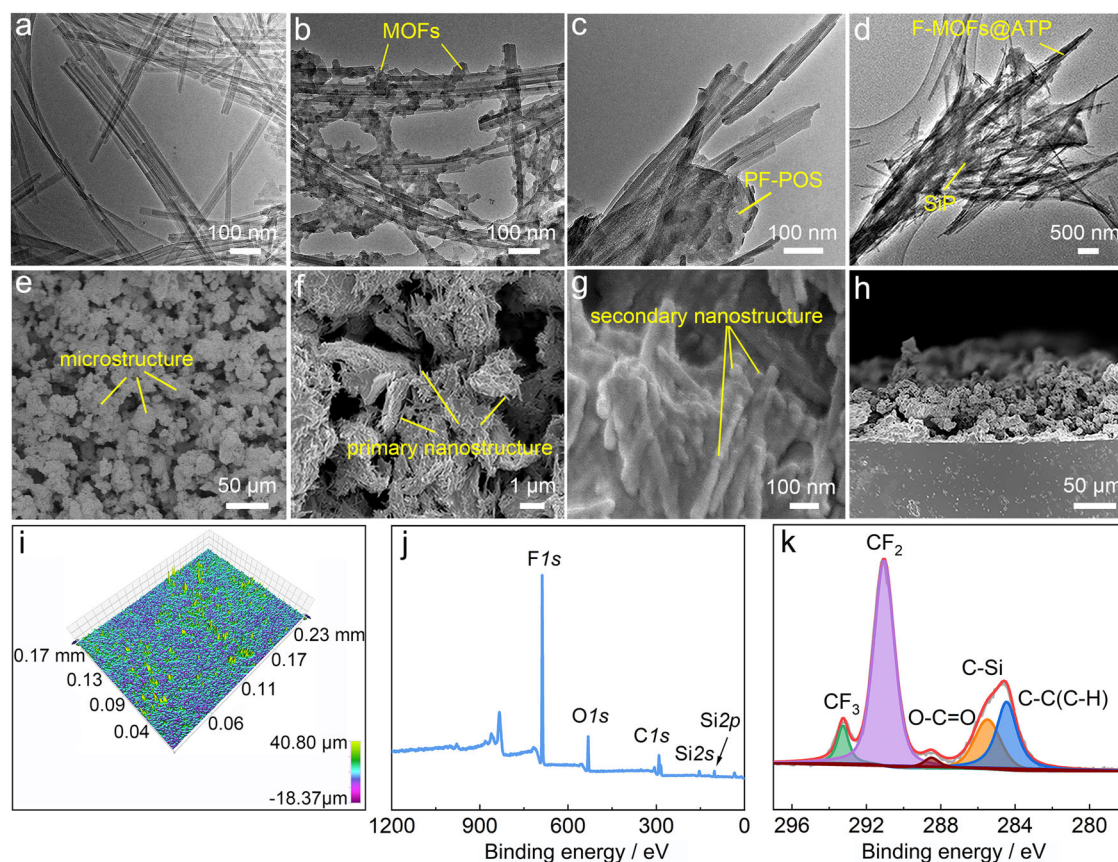

Fig. 2 | Characterization of the SiP/F-MOFs@ATP coatings. Transmission Electron Microscopic images of (**a**) ATP; (**b**) MOFs@ATP; (**c**) F-MOFs@ATP, and (**d**) the SiP/F-MOFs@ATP suspension. **e**–**g** Scanning Electron Microscopic (SEM) images, (**h**) cross-sectional SEM images, and (**i**) 3D profiler image of the SiP/F-MOFs@ATP coating. **j** X-ray Photoelectron Spectroscopy (XPS) survey spectrum and (**k**) high-resolution C 1s spectrum of the SiP/F-MOFs@ATP coating. Source data are provided as a Source Data file.

Figs. 11 and 12), and the surface energy increases gradually. Similar to the effect of ethanol content, superhydrophobicity declines slightly with an increase in the SiP adhesive content (Supplementary Fig. 13a). The mechanical robustness first increases and then decreases with increasing the SiP adhesive content (Supplementary Fig. 13b). The

coatings with 7.5 wt% or 10 wt% SiP adhesive can withstand 150 cycles Taber abrasion (125 g load, ASTM D4060). As the SiP adhesive content increases from 2.5 wt% to 12.5 wt%, the passive anti-icing performance gradually decreases (Supplementary Fig. 13c). This is mainly due to a decrease in porosity, which leads to an increase in thermal

conductivity, thus accelerating heat transfer. Additionally, the slightly decreased superhydrophobicity further diminishes the decrease of passive anti-icing performance. Note that the ethanol and SiP adhesive contents do not affect the coatings' photothermal effect (Supplementary Figs. 10e and 13d).

With increasing the coating's thickness from 87 to 227 μm, the superhydrophobicity does not change, but the mechanical robustness, passive anti-icing performance, and photothermal effect gradually get better (Supplementary Fig. 14). The improved mechanical robustness is primarily attributed to the self-similar structure of the coating. Once the surface is damaged, the newly exposed surface maintains the same morphology and chemical composition as the original surface. Additionally, the enhanced passive anti-icing performance and photothermal effect are due to the increased thermal resistance provided by a thicker coating, which effectively inhibits heat transfer. According to the above results, the SiP/F-MOFs@ATP coating (~187 μm in thickness) with 28.4 wt% ethanol and 7.5 wt% SiP adhesive was employed for further studies.

Superhydrophobicity and photothermal effect

The SiP/F-MOFs@ATP coating has a high water CA of 165.6° and a low SA of 1.8° and displays a notable silver mirror effect in water (Fig. 3a and Supplementary Fig. 15). Just a 2° tilt of the coating will cause the spherical water droplets to roll off effortlessly. The coating also exhibits good repellency against tiny water droplets of 0.5 μL (Supplementary Fig. 16). Moreover, a water jet can bounce off the coating without leaving any residue behind (Supplementary Fig. 17). A 10 μL

water droplet falling from 1.0 cm height can bounce 13 times on the coating with a solid-liquid contact duration of 14.3 ms and a bounce height of 3.7 mm in the initial impact/bounce cycle (Fig. 3b and Supplementary Movie 1). A 10 μL dirty water droplet falling from 1.0 cm height can also bounce 6 times on the coating (Supplementary Fig. 18 and Supplementary Movie 1). Furthermore, a 10 μL water droplet falling from 100 cm height can completely bounce off without any residue (Supplementary Fig. 19 and Supplementary Movie 2). Additionally, when an 8 μL water droplet on a syringe needle is moved along the coating and lifted, it does not show observable deformation (Supplementary Fig. 20). The needle-water interfacial tensile force $F_{needle-water}$ can overcome gravity of the droplet G_{water} plus the coating-water adhesion force $F_{coating-water}$ (Fig. 3c). All these outcomes demonstrate the coating's exceptional static and dynamic superhydrophobicity and very weak water adhesion on it[64,65]. Therefore, the coating has good self-cleaning performance. Water flow can completely carry away the dust on the coating (Supplementary Fig. 21). When a 60 μL water droplet rolls off the coating, it effectively removes PTFE microparticles (100 μm) adsorbed on the surface (Supplementary Fig. 22).

The SiP/F-MOFs@ATP coating can maintain good superhydrophobicity in low temperature and high RH environments, which is very important for its passive anti-icing performance. After being stored in the −10 °C and 80% RH environment for 24 h, the coating still had a low SA of ~12° even if condensation occurred on the surface (Fig. 3d and Supplementary Fig. 23). Even in the −20 °C or −30 °C and 80% RH environments for 1 h, the coating was still SH although the SA became higher (Fig. 3e, f). Note that the SA of the SiP/F-MOFs@ATP
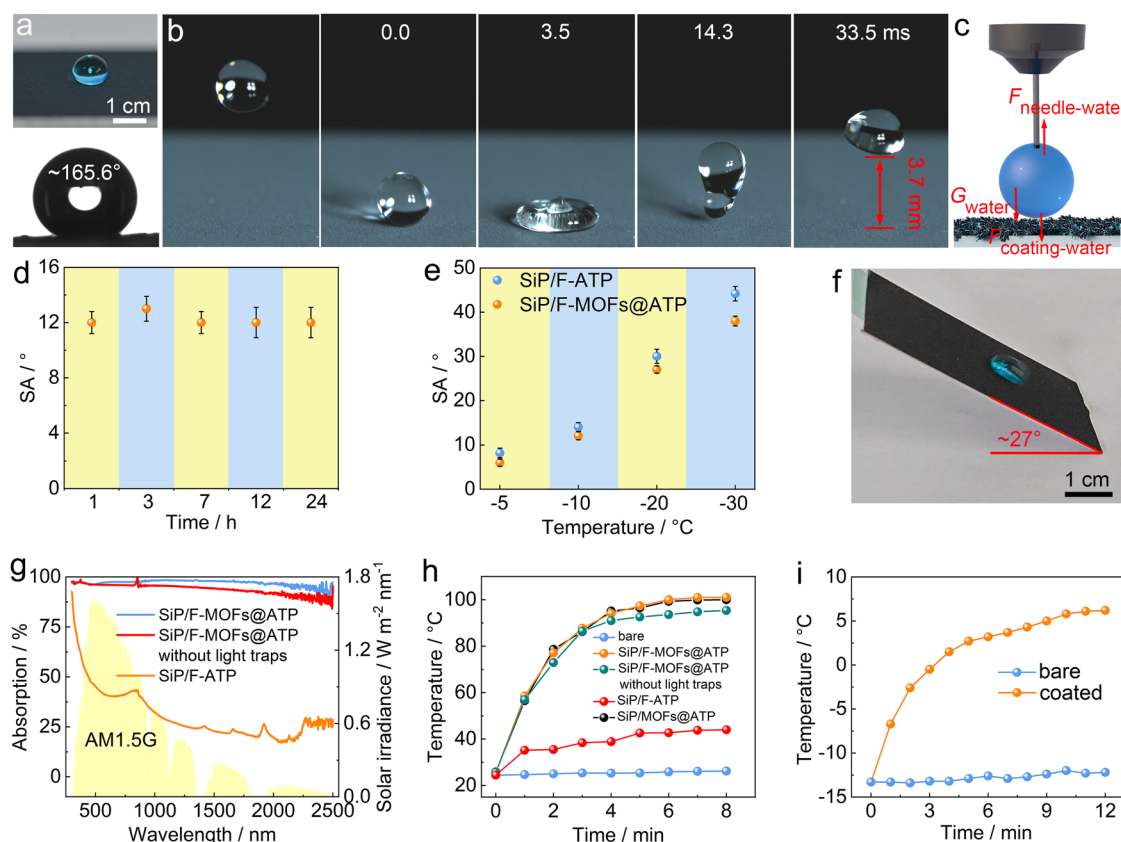

Fig. 3 | Superhydrophobicity and photothermal effect of the SiP/F-MOFs@ATP coating. Images of the coating (**a**) with water droplets (dyed blue) and (**b**) impacting by a water droplet. **c** Forces loaded on the droplet while lifting it up from the coating. SA changes of the coating (**d**) with time in the -10 °C and 80% RH environment and (**e**) with temperature after being kept in low temperature and 80% RH environments for 1 h. **f** A 60 μL water droplet (dyed blue) rolling off the coating

after being kept in the −20 °C and 80% RH environment for 1 h. **g** UV-vis-NIR spectra of various coatings. Surface temperature changes of the bare and coated Al alloy plates over time (**h**) under 1 sun in the 25.4 °C and 38% RH environment and (**i**) under 0.1 sun in the −10 °C and 80% RH environment. Data in (**d** and **e**) are shown as mean ± SD, $n = 5$. Source data are provided as a Source Data file.
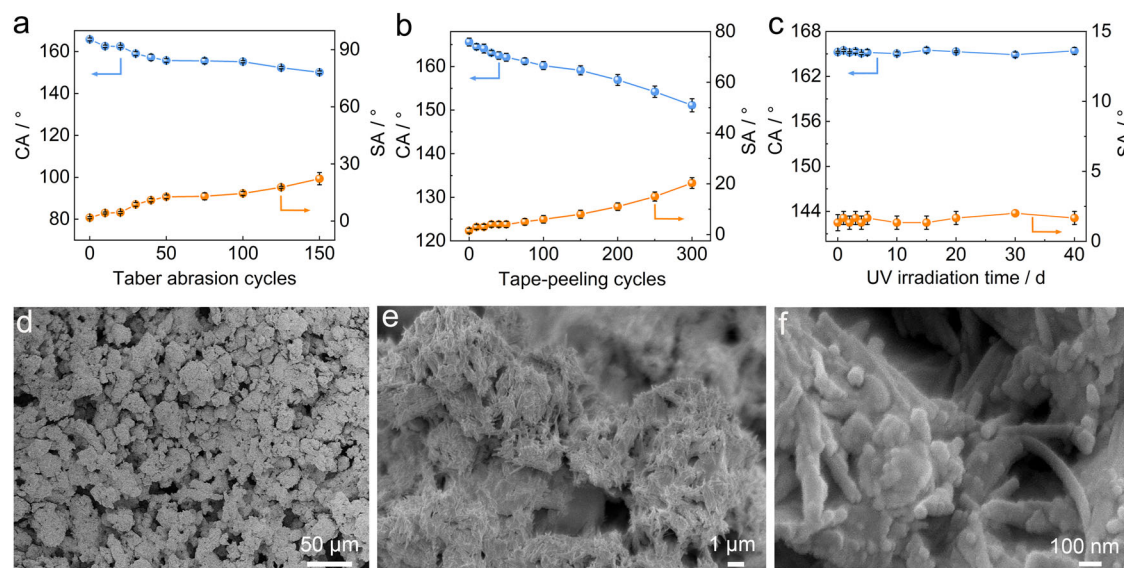
Fig. 4 | Durability of the SiP/F-MOFs@ATP coating. Changes in CA and SA of the coating during the (**a**) Taber abrasion test, (**b**) tape-peeling test, and (**c**) UV aging test. **d**–**f** SEM images of the coating after 150 cycles Taber abrasion. Data in (**a**, **b**) are shown as mean ± SD, $n = 5$. Data in (**c**) are shown as mean ± SD, $n = 3$. Source data are provided as a Source Data file.

coating is lower than the SiP/F-ATP coating with two-tier micro-/nanostructure. Thus, the MOFs as the secondary nanostructure can enhance superhydrophobicity of the SiP/F-MOFs@ATP coating in low temperature and high RH environments. This is attributed to the synergistic effect of the SiP/F-MOFs@ATP coating's three-tier micro-/nano-/nanostructure and low surface energy. So, the condensed microdroplets are in the nano-Cassie state rather than the Wenzel state on the coating's surface[66]. The nano-Cassie state can recover to the micro-Cassie state[66]. This was further confirmed by the anti-condensation tests. The superhydrophobicity decreased after condensation, but fully recovered when the coating was left at room conditions for 1 h (Supplementary Fig. 24). Also, the condensed microdroplets could be carried away by rolling water droplets (Supplementary Movie 3). The SiP/F-MOFs@ATP coating has excellent anti-condensation performance compared with recent studies (Supplementary Table 5)[67–69].

The SiP/F-MOFs@ATP coating shows strong light absorption of ~97.32% in the 300−2500 nm wavelength region and excellent photothermal effect compared with the SiP/F-ATP SH coating and the flat SiP/F-MOFs@ATP hydrophobic coating without light traps (CA = 111°, Fig. 3g–i and Supplementary Fig. 25). Under 1 sun irradiation in the 25.4 °C and 38% RH environment, the SiP/F-MOFs@ATP and SiP/MOFs@ATP coatings' surface temperature increases from room temperature to 101 °C in 8 min, which surpasses most photothermal SH coatings (Fig. 3h, Supplementary Fig. 26a and Supplementary Table 6). This result also indicates that PF-POS has no influence on the photothermal effect (Fig. 3h). Furthermore when light irradiates on the SiP/F-MOFs@ATP coated cylindrical cable line, the temperature of the directly irradiated area rises rapidly, the heat gradually propagates downward along the surface, and eventually reaches the un-irradiated area (Supplementary Movie 4). Nonetheless, in cold weather where icing often happens, typically the solar flux is low (<0.5 sun), the ambient temperature is <0 °C and the RH is high (>50%) (Supplementary Table 2). Such environments will lead to failure of anti-icing and de-icing of most photothermal SH coatings due to insufficient photothermal effect. Fortunately, the SiP/F-MOFs@ATP coating continues to show good photothermal effect in such environments. Its surface temperature quickly rises from −13.3 °C to 1.5 °C in 4 min and further rise to 6.1 °C in 11 min under 0.1 sun in the −10 °C and 80% RH environment (Fig. 3i and Supplementary Fig. 26b). Note that such

photothermal effect test is rare in the literature, yet very important for practical anti-icing and de-icing of photothermal SH coatings[32].

The strong light absorption and excellent photothermal effect of the SiP/MOFs@ATP coating are due to presence of numerous MOFs nanoparticles (1 at.% Cu, EDS analysis) with excellent photothermal conversion efficiency on its surface (Supplementary Fig. 5 and Supplementary Table 7)[30]. Additionally, the coating with three-tier micro-/nano-/nanostructure has numerous light traps (Fig. 2e, f). A greater amount of incident light is absorbed in the light traps through multiple internal scattering, thereby slightly enhancing the photothermal performance[70].

Mechanical robustness and chemical/weather resistance

The SiP/F-MOFs@ATP coating has excellent mechanical robustness according to the Taber abrasion test (125 g load, CS 10 grinding wheel, ASTM D4060), the tape-peeling test (11 kPa load, 3 M tape, ASTM D3359) and the sand drop test from 10 cm height (ASTM D968). The CA dropped and the SA rose gradually during these tests, but the coating remained SH after 150 cycles Taber abrasion, 300 cycles tape-peeling, or 650 g of sand particle impact (Fig. 4a, b and Supplementary Figs. 27–28). Moreover, the coating could even withstand hand rubbing and brush under water as well as 5 min ultrasonic treatment in various organic solvents (Supplementary Fig. 29 and Supplementary Movie 5). The coating could also maintain the original mechanical robustness after immersion in 0.1 M NaOH(aq) for 30 min or treatment at 150 °C/−30 °C in the air for 1 h (Supplementary Fig. 30). Additionally, the coating has good adhesion strength on the Al alloy plate according to the hundred-grid adhesion strength test (ASTM D3359, Supplementary Fig. 31).

The coating's mechanical robustness outstrips most SH coatings due to the following facts. (i) The hydrophobic SiP adhesive with high hardness and its controlled phase separation can enhance binding of the coating to the substrate and binding among the F-MOFs@ATP nanorods in the coating without affecting superhydrophobicity and photothermal effect of F-MOFs@ATP[50]. (ii) The coating's self-similar micro-/nano-/nanostructure warrants almost unchanged morphology and chemical composition after abrasion or tape-peeling (Fig. 4d–f and Supplementary Fig. 32)[17]. (iii) The ATP nanorods with high aspect ratio also contribute to the excellent mechanical robustness[71]. Replacing the ATP nanorods with granular SiO₂ nanoparticles caused significant
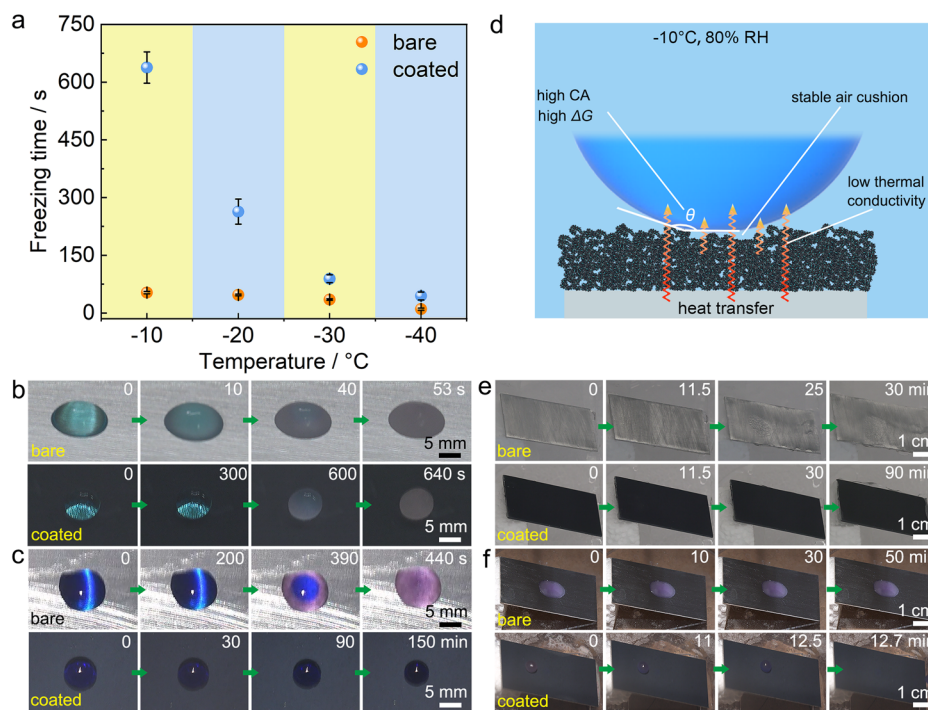
Fig. 5 | Passive anti-icing and active de-icing performance of the SiP/F-MOFs@ATP coating. a Static freezing time of water droplets on the bare and coated Al alloy plates in the environments of different ambient temperature and 80% RH without sunlight. Static icing process of water droplets on the bare and coated Al alloy plates in the −10 °C and 80% RH environment (**b**) without sunlight and (**c**) under 0.1 sun. **d** Passive anti-icing mechanism of the coating. **e** Dynamic icing process of water droplets on the bare and coated Al alloy plates in the −10 °C and 80% RH environment without sunlight. **f** Active de-icing process of frozen water droplets on the bare and coated Al alloy plates in the −10 °C and 80% RH environment under 0.1 sun. Water in (**b**, **c**) and (**f**) are dyed blue. Data in (**a**) are shown as mean ± SD, *n* = 5. Source data are provided as a Source Data file.

decrease in mechanical robustness (Supplementary Fig. 33). Note that the coating's mechanical robustness is still lower than a few state-of-the-art SH coatings (Supplementary Table 8), as superhydrophobicity, mechanical robustness and passive anti-icing performance are taken into account simultaneously here to achieve good anti-icing performance in real conditions.

The SiP/F-MOFs@ATP coating also has excellent UV aging stability. After 40 days UV aging (365 nm, 12 W), the superhydrophobicity showed negligible change (Fig. 4c and Supplementary Fig. 34). This is primarily due to excellent stability of the SiP adhesive and PF-POS as well as cover of the MOFs@ATP nanorods by PF-POS[17].

Passive anti-icing and active de-icing performances

The SiP/F-MOFs@ATP coating shows excellent static passive anti-icing performance, surpassing most photothermal SH coatings (Supplementary Table 9). In the −10 °C and 80% RH environment without sunlight (simulated outdoor environment at night in winter), the water (60 μL) freezing time was only 53 s on the Al alloy plate but delayed to 640 s on the coated plate, although they have similar surface temperature (Fig. 5a, b, Supplementary Fig. 35a, b and Supplementary Movie 6). This effect of the coating can also be seen in colder environments. For example, the freezing time at −40 °C was prolonged from 10 s to 58 s by the coating. Additionally, water droplets did not freeze on the coated Al alloy plate in 150 min in the 0 °C and 80% RH environment without sunlight (Supplementary Fig. 36). In the −10 °C and 80% RH environment with weak sunlight (0.1 sun, simulated outdoor environment at daytime in winter), water droplets completely froze in 440 s on the Al alloy plate because its surface temperature remained at about −10 °C, but could not freeze at all on the coated plate in 150 min because its surface temperature rapidly increased to >0 °C (Fig. 5c, Supplementary Fig. 35c, d and Supplementary Movie 7). In addition,

the ice adhesion strength on the Al alloy plate was 205.3 kPa, which was reduced to 36.3 kPa by the coating as measured by directly removing the ice in the frozen state (Supplementary Fig. 37). Moreover, the coating maintained its superhydrophobicity and ice adhesion strength over twenty freezing/de-icing cycles, with no significant alterations in surface morphology (Supplementary Fig. 38). This performance demonstrates its excellent cyclic freezing/de-icing stability.

The coating's excellent static passive anti-icing performance is due to the following facts (Fig. 5d). (i) The ΔG of icing is high on the coating with high superhydrophobicity and thus ice nucleation is greatly inhibited according to the classical nucleation theory[51]. (ii) At the solid-liquid interface there is a stable air cushion and the actual contact area of water droplets with the coating is extremely low (3.4%) according to the Cassie-Baxter equation, which effectively prevents heat transfer from the coating to water and reduces the ice adhesion strength[52]. (iii) The coating can inhibit heat transfer from the Al alloy plate to water due to its low thermal conductivity (0.19 W m^{-1} K^{-1})[52]. (iv) The coating has excellent photothermal effect. These interpretations were further confirmed by the COMSOL simulated calculation about the time required for the decrease of water droplets' (60 μL, on various surfaces) temperature from 0 °C to −10 °C in the −10 °C and 80% RH environment (Supplementary Note, Supplementary Fig. 39 and Supplementary Tables 10 and 11). The water droplet on the SiP/F-MOFs@ATP coated Al alloy plate needed a much longer time. The water droplet's temperature on the coated plate even increased to -5 °C under 0.1 sun.

The SiP/F-MOFs@ATP coating also shows excellent dynamic passive anti-icing performance according to the continuous water dropping test (0 °C, ~40 μL droplets, 50-60 droplets per min) from 10 cm height onto the 20° tilted Al alloy plates or horizontal cable lines in the −10 °C and 80% RH environment without sunlight. Ice started to
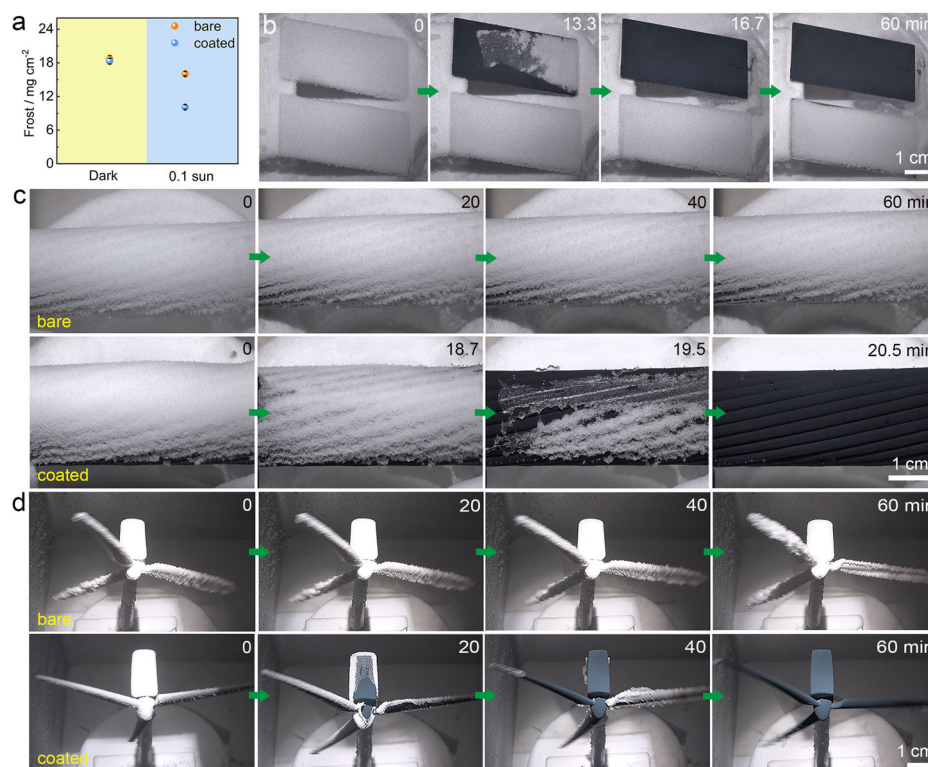
Fig. 6 | Passive anti-frosting and active de-frosting performance of the SiP/F-MOFs@ATP coating. a Frost content on the bare and coated Al alloy plates after 30 min frosting test without sunlight or under 0.1 sun. De-frosting process on the bare and coated (**b**) Al alloy plates, (**c**) cable lines, and (**d**) wind turbine blade models in the −10 °C and 80% RH environment under 0.1 sun. The frost is -0.8 mm in thickness in (**b**). Data in (**a**) are shown as mean ± SD, $n = 5$. Source data are provided as a Source Data file.

progressively form on the Al alloy plate after 11.5 min and a large amount of ice formed after 30 min, but no ice formed on the coated plate even after 90 min (Fig. 5e and Supplementary Movie 8). Also, ice formed immediately on the cable line, and many icicles formed after 30 min, but most water droplets bounced off the coated cable line and only a few subcooled droplets progressively adhered on it in 60 min (Supplementary Fig. 40 and Supplementary Movie 9). The excellent dynamic passive anti-icing performance of the coating is due to the fact that most water droplets bounce or roll off it quickly before their temperature drops below the freezing point[51].

Furthermore, the SiP/F-MOFs@ATP coating shows good active de-icing performance in low temperature, high RH, and weak sunlight environments. In the −10 °C and 80% RH environment under 0.1 sun, the frozen water droplet (60 μL) on the Al alloy plate did not melt even after 50 min because its surface temperature maintained at about −10 °C, but that on the coated plate (-20° tilted) melted and rolled off after 12.7 min because its surface temperature rapidly increased to >0 °C (Fig. 5f, Supplementary Fig. 35e, f and Supplementary Movie 10). In the same environment under 0.3 sun, the icicle on the cable line did not melt at all in 60 min, but that on the coated cable line melted and fell off after 28 min (Supplementary Fig. 41 and Supplementary Movie 11). The coating's active de-icing performance surpasses most photothermal SH coatings (Supplementary Table 12). Furthermore, the coating has excellent freezing/photothermal de-icing cycling stability. The coating could maintain the original morphology, super-hydrophobicity, and photothermal de-icing performance after five freezing/de-icing cycles (Supplementary Fig. 42).

The coating's good active de-icing performance is attributed to the excellent superhydrophobicity and photothermal effect in low temperature, high RH, and weak sunlight environments[21], combined with its low thermal conductivity. The coating absorbs light and converts it into heat to increase its surface temperature. When the surface

temperature rises above 0 °C, ice on the coating begins to melt and then rolls off due to its excellent superhydrophobicity. These interpretations were further firmed by the COMSOL simulated calculation (Supplementary Note, Supplementary Fig. 43, Supplementary Tables 11 and 13). For the SiP/F-MOFs@ATP coated Al alloy plate, the temperature of the frozen water droplet increased to >0 °C after 1.6 min and rolled off under the action of gravity after 8.2 min in the −10 °C and 80% RH environment under 0.1 sun.

Passive anti-frosting and active de-frosting performances

Frosting is also common in low temperature and high RH environments, which may cause failure of anti-icing performance of SH coatings due to condensation of supercooled water in their surface structure[30]. So, the passive anti-frosting performance of the SiP/F-MOFs@ATP coating was studied by spraying supercooled water mist using a humidifier (1.67 g min⁻¹) onto it in the −30 °C and >80% RH environment without sunlight. Although both the bare and coated Al alloy plates were eventually covered with frost after 30 min, there was slightly less frost on the coated one (18.7 vs 18.3 mg cm⁻², Fig. 6a and Supplementary Movie 12). Differently, under 0.1 sun weak sunlight, the frost on the coated Al alloy plate was much less than that on the bare one after 30 min (16.0 vs 10.1 mg cm⁻², Fig. 6a and Supplementary Movie 13). The anti-frosting performance was further studied on a −5 °C cooling plate in 0 °C and 80% RH environment under 0.3 sun. The Al alloy plate was completely covered by condensed frost after 25 min, but the coated Al alloy plate was almost free of frost (Supplementary Fig. 44). Thus, the coating has good passive anti-frosting performance, as it can delay/inhibit frost formation and propagation by (i) promoting jumping off of the subcooled water mist before nucleation originating from its good superhydrophobicity to tiny water droplets (Supplementary Fig. 16)[72], (ii) the excellent photothermal effect and (iii) low thermal conductivity.

The SiP/F-MOFs@ATP coating shows good active de-frosting performance compared with most photothermal SH coatings (Supplementary Table 14). In the −10 °C and 80% RH environment under 0.1 sun weak sunlight, the frost -0.8 mm in thickness on the 20° tilted Al alloy plate and SiP/F-ATP coated plate did not melt in 60 min, but that on the SiP/F-MOFs@ATP coated plate melted and rolled off in 16.7 min (Fig. 6b, Supplementary Fig. 45 and Supplementary Movie 14). The thinner the frost, the shorter the de-frosting time is. The frost -0.5 mm in thickness melted in 12.2 min (Supplementary Fig. 46). This is because light can penetrate the frost layer and convert into heat (Supplementary Fig. 47), causing the frost layer to thin out and thus the solar flux behind the frost to increase. When the frost becomes very thin, the solar flux behind the frost increases rapidly, i.e., complete melt of frost.

The SiP/F-MOFs@ATP coating also shows good active de-frosting performance on cable lines and wind turbine blade models. The frost on the bare cable line did not melt in 60 min under 0.1 sun, but that on the coated one completely melted after 20.5 min (Fig. 6c and Supplementary Movie 15). Similar phenomena were observed for the rotating (7.2 km h^{-1}) wind turbine blades but required more irradiation time (60 min) as rotation accelerated heat transfer between the blades and the environment (Fig. 6d and Supplementary Movie 16). Moreover, active de-frosting was also achieved in colder environments (−20 and −30 °C) under stronger sunlight of 0.3–0.7 sun (Supplementary Fig. 48 and Supplementary Movies 17, 18).

Performances in winter outdoor environments

The performances of the SiP/F-MOFs@ATP coating in winter outdoor environments were thoroughly evaluated in Lanzhou, Gansu, PR China. The coating shows excellent static passive anti-icing performance in −12 °C and 50% RH environment without sunlight. The water (60 μL) freezing time was 105 s on the Al alloy plate but delayed to 660 s on the coated one (Supplementary Fig. 49 and Supplementary Movie 19), although they have similar surface temperature of about −12 °C in the freezing process.

The coating shows excellent dynamic passive anti-icing performance in −11 °C and 50% RH environment without sunlight. Many icicles formed on the cable line after continuous dropping of supercooled water (0 °C) for 25 min, but only a few droplets adhered on the coated cable line (Supplementary Fig. 50 and Supplementary Movie 20), although they have similar surface temperatures in the icing process.

The coating shows excellent passive anti-snowing and photothermal anti-snowing performance in the real snowing process (Supplementary Fig. 51a). On the Al alloy plate, snow accumulated immediately and continuously although there was -0.03 sun irradiation after 1.5 h, and there was a large amount of snow after 2.4 h (Supplementary Fig. 52 and Supplementary Movie 21). In contrast, on the coated Al alloy plate there was only a small amount of snow after 1.5 h and snow accumulation ceased and gradually melted when there was -0.03 sun irradiation due to the photothermal effect, i.e., higher surface temperature. After 2.4 h, there was no snow on the coated sample.

The coating shows good active de-icing performance in winter outdoor environments (Supplementary Fig. 51b). The icicle on the cable line did not melt at all in 20 min, but the few frozen droplets on the coated cable line melted and fell off after 16.7 min (Supplementary Fig. 53 and Supplementary Movie 22). The surface temperature of the cable line maintained at about −5 °C, but that of the coated cable line increased continuously to 0.7 °C after 10 min and to 1.6 °C after 20 min. Furthermore, in the real environment (Supplementary Fig. 51c), the accumulated snow on the Al alloy did not melt at all in 36 min, but that on the coated Al alloy melted completely due to its obviously higher surface temperature (Supplementary Fig. 54 and Supplementary Movie 23).

Large-scale preparation

Scalable fabrication is essential for practical uses of the photothermal SH SiP/F-MOFs@ATP coating for anti-icing and de-icing. As the raw materials are readily available at a reasonable cost and the preparation process is straightforward, we have achieved large-scale preparation of the SiP/F-MOFs@ATP suspension (50 L d^{-1}). We have also prepared the SiP/F-MOFs@ATP coating in large size (100 cm × 50 cm, Supplementary Fig. 55), as it can be fabricated by just one-step spraying and room temperature curing. Moreover, the large coating shows almost the same superhydrophobicity (CA > 165°, SA < 2°), photothermal effect, mechanical robustness, and anti-icing/de-icing performance as that prepared at the laboratory scale (Supplementary Fig. 56). The SiP/F-MOFs@ATP suspension costs 48.6 USD L^{-1}, which can form 6–8 m^2 of the coating with a cost of only 6.1–8.1 USD m^{-2}.

Slight sedimentation of the SiP/F-MOFs@ATP suspension will happen after a long storage time (e.g., 14 days), which can be made uniform again simply by magnetically stirring for 5 min. The coating with the same performance can be obtained using the redispersed suspension (Supplementary Fig. 57). Moreover, the coating can be applied onto flexible ABS plates with lower thermal conductivity. Compared to the coating on the Al alloy plate, the coating on the ABS plate exhibits (i) comparable superhydrophobicity and mechanical robustness, and (ii) better photothermal and passive anti-icing performances due to the lower thermal conductivity of the ABS plate (Supplementary Figs. 58 and 31).

In summary, to solve the drawbacks of traditional superhydrophobic coatings for anti-icing, we suggested the design criteria of robust photothermal superhydrophobic coatings and subsequently achieved their large-scale preparation. In simulated/real icing environments with low temperatures, high humidity, and weak sunlight, the coatings obviously outperform their counterparts in terms of comprehensive performances (Supplementary Table 15). This is ascribed to the synergistic effect of multiple factors, e.g., self-similar three-tier micro-/nano-/nanostructures with low surface energy, low thermal conductivity, nanosized MOFs, numerous light traps, phase-separated adhesive, and reinforcement by attapulgite (Supplementary Table 16). Especially, introduction of nanosized MOFs as the secondary nanostructure not only imparts excellent photothermal performance to the coating but also further improves the coating's superhydrophobicity in low-temperature and high-humidity environments. Consequently, the coatings show exceptional anti-icing/frosting and de-icing/frosting properties in simulated/real icing environments. In the future, the coatings' overall performances should be further improved in order to realize widespread real-world applications for anti-icing/de-icing on various infrastructures. Replacing ATP nanorods and MOFs with other nanomaterials is a possible strategy. We anticipate that the findings here will help advance the design, preparation, and applications of photothermal superhydrophobic coatings.

Methods
Synthesis of MOFs@ATP nanorods

9.7 g of Cu(NO$_3$)$_2$ and 6.5 g of HHTP were sequentially added into 1 L of the N,N-dimethylformamide/H$_2$O mixture (v/v = 1/10) and stirred for 10 min. Then, 25 g of the ATP nanorods were added into the above solution and stirred in a water bath (85 °C, 500 rpm) for 15 h to form the MOFs@ATP suspension. Finally, the MOFs@ATP nanorods were obtained by filtration and drying in an oven at 85 °C.

Preparation of F-MOFs@ATP nanorods

10 g of the MOFs@ATP nanorods were dispersed in 1 L of ethanol/water/ammonia solution by stirring for 10 min followed by ultrasonication for 1 min at room temperature. Then, PFDTES (8 mL) and TEOS (1 mL) were added into the above suspension. After reaction at room temperature for 2 h under stirring, the F-MOFs@ATP suspension

was formed. Finally, the semi-solid F-MOFs@ATP nanorods with absorbed ethanol were obtained by centrifugation at 1770 × g.

Fabrication of photothermal SH SiP/F-MOF@ATP coatings

First, a proper amount of the SiP adhesive was dissolved in 572 g of dimethyl carbonate by stirring for 5 min at room temperature. 263 g of the semi-solid F-MOFs@ATP nanorods (30 wt%) were slowly added into the SiP adhesive solution under stirring. Then, a proper amount of ethanol was added slowly into the suspension to adjust phase separation degree of the SiP adhesive. After vigorous stirring for 3 h, the uniform SiP/F-MOF@ATP suspension was obtained. The SiP/F-MOF@ATP coatings were readily prepared by spraying the suspension (4 mL) onto the substrates (12 cm^2) and curing at room temperature for 24 h. The SiP/F-MOF@ATP suspension in large volume and the coatings in large size were prepared via the same procedure.

The additional experimental information including materials, mechanical robustness tests, passive anti-icing and anti-frosting tests, active de-icing and de-frosting tests and characterization is available in the Supplementary Information.

Data availability

The data that support the findings of this study are available within the paper and Supplementary Information. Source data are provided with this paper.

References

1. Lambley, H. et al. Freezing-induced wetting transitions on super-hydrophobic surfaces. *Nat. Phys.* **19**, 649–655 (2023).
2. Li, Q. & Guo, Z. Fundamentals of icing and common strategies for designing biomimetic anti-icing surfaces. *J. Mater. Chem. A* **6**, 13549–13581 (2018).
3. Kreder, M. J., Alvarenga, J., Kim, P. & Aizenberg, J. Design of anti-icing surfaces: smooth, textured or slippery? *Nat. Rev. Mater.* **1**, 15003 (2016).
4. Moral, J. et al. A holistic solution to icing by acoustic waves: de-icing, active anti-icing, sensing with piezoelectric crystals, and synergy with thin film passive anti-icing solutions. *Adv. Funct. Mater.* **33**, 2209421 (2023).
5. Li, Y. et al. Solar deicing nanocoatings adaptive to overhead power lines. *Adv. Funct. Mater.* **32**, 2113297 (2022).
6. Wang, L. et al. Robust anti-icing performance of a flexible super-hydrophobic surface. *Adv. Mater.* **28**, 7729–7735 (2016).
7. Li, J., Ueda, E., Paulssen, D. & Levkin, P. A. Slippery lubricant-infused surfaces: properties and emerging applications. *Adv. Funct. Mater.* **29**, 1802317 (2019).
8. Fang, X. et al. Novel SLIPS based on the photo-thermal MOFs with enhanced anti-icing/de-icing properties. *RSC Adv.* **12**, 13792–13796 (2022).
9. Liu, K. et al. Janus effect of antifreeze proteins on ice nucleation. *Proc. Natl Acad. Sci. USA* **113**, 14739–14744 (2016).
10. Garnham, C. P., Campbell, R. L. & Davies, P. L. Anchored clathrate waters bind antifreeze proteins to ice. *Proc. Natl Acad. Sci. USA* **108**, 7363–7367 (2011).
11. Ru, Y. et al. Reversibly thermosecreting organogels with switchable lubrication and anti-icing performance. *Angew. Chem. Int. Ed.* **59**, 11876–11880 (2020).
12. He, Z. et al. Bioinspired multifunctional anti-icing hydrogel. *Matter* **2**, 723–734 (2020).
13. Wang, L. et al. Spontaneous dewetting transitions of droplets during icing & melting cycle. *Nat. Commun.* **13**, 378 (2022).
14. Li, L. et al. Challenges and strategies for commercialization and widespread practical applications of superhydrophobic surfaces. *Sci. Adv.* **9**, eadj1554 (2023).
15. Lv, J., Song, Y., Jiang, L. & Wang, J. Bio-inspired strategies for anti-icing. *ACS Nano* **8**, 3152–3169 (2014).
16. Zhang, S. et al. Bioinspired surfaces with superwettability for anti-icing and ice-phobic application: concept, mechanism, and design. *Small* **13**, 1701867 (2017).
17. Wei, J. et al. Scalable robust superamphiphobic coatings enabled by self-similar structure, protective micro-skeleton, and adhesive for practical anti-icing of high-voltage transmission tower. *Adv. Funct. Mater.* **32**, 2206014 (2022).
18. Zhu, T. et al. A transparent superhydrophobic coating with mechanochemical robustness for anti-icing, photocatalysis and self-cleaning. *Chem. Eng. J.* **399**, 125746 (2020).
19. Xie, Z. et al. Recent progress in anti-icing and deicing applications of the photothermal conversion materials. *Prog. Org. Coat.* **184**, 107834 (2023).
20. Cong, Q. et al. Research progress of superhydrophobic materials in the field of anti-/de-icing and their preparation: a review. *Materials* **16**, 5151 (2023).
21. Jiang, G., Chen, L., Zhang, S. & Huang, H. X. Superhydrophobic SiC/CNTs coatings with photothermal deicing and passive anti-icing properties. *ACS Appl. Mater. Interfaces* **10**, 36505–36511 (2018).
22. Wu, S. et al. Superhydrophobic photothermal icephobic surfaces based on candle soot. *Proc. Natl Acad. Sci. USA* **117**, 11240–11246 (2020).
23. Zheng, W. et al. Magnetic responsive and flexible composite superhydrophobic photothermal film for passive anti-icing/active deicing. *Chem. Eng. J.* **427**, 130922 (2022).
24. Li, N. et al. Micro/nano-cactus structured aluminium with super-hydrophobicity and plasmon-enhanced photothermal trap for ice-phobicity. *Chem. Eng. J.* **429**, 132183 (2022).
25. Zhao, Y. et al. Multifunctional Ti$_3$C$_2$T$_x$ Mxene-based composite coatings with superhydrophobic anti-icing and photothermal deicing properties. *ACS Appl. Mater. Interfaces* **14**, 26077–26087 (2022).
26. Cheng, T. et al. Magnetic particle-based super-hydrophobic coatings with excellent anti-icing and thermoresponsive deicing performance. *J. Mater. Chem. A* **3**, 21637–21646 (2015).
27. Li, D., Ma, L., Zhang, B. & Chen, S. Facile fabrication of robust and photo-thermal super-hydrophobic coating with efficient ice removal and long-term corrosion protection. *Chem. Eng. J.* **450**, 138429 (2022).
28. Liu, Y. et al. Robust photothermal coating strategy for efficient ice removal. *ACS Appl. Mater. Interfaces* **12**, 46981–46990 (2020).
29. Guo, C. et al. Development of flexible photothermal super-hydrophobic microarray by photolithography technology for anti-icing and deicing. *Prog. Org. Coat.* **182**, 107675 (2023).
30. Zhang, L. et al. Highly efficient photothermal icephobic/de-icing MOF-based micro and nanostructured surface. *Adv. Sci.* **10**, 325703 (2023).
31. Zhou, M. et al. Robust photothermal icephobic surface with mechanical durability of multi-bioinspired structures. *Adv. Mater.* **35**, 2305322 (2023).
32. Wu, Y. et al. Recent advancements in photothermal anti-icing/deicing materials. *Chem. Eng. J.* **469**, 143924 (2023).
33. Xu, J., Gong, X. & Ramakrishna, S. Robust photothermal anti-icing/deicing via flexible CMDSP carbon nanotube films. *Nanotechnology* **33**, 325703 (2022).
34. Li, S. et al. A sustainable superhydrophobic and photothermal coatings for anti-icing application on concrete with a simple method for CNTs/SiO$_2$ modification. *Sustainability* **15**, 15865 (2023).
35. Li, J. et al. Superhydrophobic coating with a micro- and nano-sized MnO$_2$/PDMS composite structure for passive anti-icing/active de-icing and photothermal applications. *J. Mater. Chem. C* **11**, 15443–15453 (2023).
36. Wei, X., Wei, J., Feng, Y. & Wang, J. Photothermal hydrophobic coating with light-trapping and thermal isolated effects for efficient

photothermal anti-icing/de-icing. *Prog. Org. Coat.* **179**, 107550 (2023).

37. He, Z. et al. Electro-/photo-thermal promoted anti-icing materials: A new strategy combined with passive anti-icing and active de-icing. *Adv. Mater. Interfaces* **9**, 2200275 (2022).

38. Zhang, W. et al. Robust superhydrophobicity: mechanisms and strategies. *Chem. Soc. Rev.* **50**, 4031–4061 (2021).

39. Verho, T. et al. Mechanically durable superhydrophobic surfaces. *Adv. Mater.* **23**, 673–678 (2011).

40. Wang, D. et al. Design of robust superhydrophobic surfaces. *Nature* **582**, 55–59 (2020).

41. Ye, H. et al. Durable and robust self-healing superhydrophobic Co-PDMS@ZIF-8-coated MWCNT films for extremely efficient emulsion separation. *ACS Appl. Mater. Interfaces* **11**, 38313–38320 (2019).

42. Li, X. et al. Self-healing superhydrophobic conductive coatings for self-cleaning and humidity-insensitive hydrogen sensors. *Chem. Eng. J.* **410**, 128353 (2021).

43. Zhang, R. et al. Facile preparation of robust superamphiphobic coatings on complex substrates via nonsolvent-induced phase separation. *ACS Appl. Mater. Interfaces* **14**, 49047–49058 (2022).

44. Deng, X., Mammen, L., Butt, H.-J. & Vollmer, D. Candle soot as a template for a transparent robust superamphiphobic coating. *Science* **335**, 67–70 (2012).

45. Zhang, H. et al. A skin-inspired design integrating mechano–chemical–thermal robustness into superhydrophobic coatings. *Adv. Mater.* **34**, 2203792 (2022).

46. Lu, Y. et al. Robust self-cleaning surfaces that function when exposed to either air or oil. *Science* **347**, 1132–1135 (2015).

47. Gu, W. et al. Ultra-durable superhydrophobic cellular coatings. *Nat. Commun.* **14**, 5953 (2023).

48. Liu, Z., Hu, J. & Jiang, G. Superhydrophobic and photothermal deicing composite coating with self-healing and anti-corrosion for anti-icing applications. *Surf. Coat. Tech.* **444**, 128668 (2022).

49. Wang, P. et al. A superhydrophobic/electrothermal/photothermal synergistically anti-icing strategy with excellent self-healable and anti-abrasion property. *J. Bionic Eng.* **18**, 1147–1156 (2021).

50. Wei, J. et al. Durable superhydrophobic coatings for prevention of rain attenuation of 5G/weather radomes. *Nat. Commun.* **14**, 2862 (2023).

51. Li, W., Zhan, Y. & Yu, S. Applications of superhydrophobic coatings in anti-icing: theory, mechanisms, impact factors, challenges and perspectives. *Prog. Org. Coat.* **152**, 106117 (2021).

52. Chang, S., Qi, H., Zhou, S. & Yang, Y. Experimental and numerical study on freezing process of water droplets under surfaces with different wettability. *Appl. Therm. Eng.* **219**, 119516 (2023).

53. Pan, S. et al. Coatings super-repellent to ultralow surface tension liquids. *Nat. Mater.* **17**, 1040–1047 (2018).

54. Li, X.-M., Reinhoudt, D. & Crego-Calama, M. What do we need for a superhydrophobic surface? A review on the recent progress in the preparation of superhydrophobic surfaces. *Chem. Soc. Rev.* **36**, 1350–1368 (2007).

55. Gao, X., Tian, J., Zhang, Y. & Zhu, J. Superhydrophobic heat insulating coating used in construction, aerospace and warehousing, comprises water body set with superhydrophobic porous film and solid low thermal conductivity phase material. Patent CN104974581-A; CN104974581-B.

56. Sun, X., Zhao, X. & Yang, F. Thermal conductivity of bulk attapulgite prepared by pressureless sintering. *J. Shanghai Jiaotong Univ.* **57**, 194 (2023).

57. Yong, J. et al. Superoleophobic surfaces. *Chem. Soc. Rev.* **46**, 4168–4217 (2017).

58. Chu, Z. & Seeger, S. Superamphiphobic surfaces. *Chem. Soc. Rev.* **43**, 2784–2798 (2014).

59. Xie, H. et al. Non-fluorinated and durable photothermal super-hydrophobic coatings based on attapulgite nanorods for efficient anti-icing and deicing. *Chem. Eng. J.* **428**, 132585 (2022).

60. Wu, L. et al. Magnetic, durable, and superhydrophobic polyurethane@Fe$_3$O$_4$@SiO$_2$@fluoropolymer sponges for selective oil absorption and oil/ water separation. *ACS Appl. Mater. Interfaces* **7**, 4936–4946 (2015).

61. Sakthivel, R. et al. Rapid oil-water separation using modified non-woven viscose fabrics. *Mater. Chem. Phys.* **312**, 128645 (2024).

62. He, H., Huang, W. & Guo, Z. Superhydrophobic and photothermal SiC/TiN durable composite coatings for passive anti-icing/active de-icing and de-frosting. *Mater. Today Phys.* **30**, 100927 (2023).

63. Dong, K. et al. Superhydrophobic coating based on organic/inor-ganic double component adhesive and functionalized nano-particles with good durability and anti-corrosion for protection of galvanized steel. *Colloid Surf. A* **640**, 128360 (2022).

64. Liu, M., Li, J., Hou, Y. & Guo, Z. Inorganic adhesives for robust superwetting surfaces. *ACS Nano* **11**, 1113–1119 (2017).

65. Lin, D. et al. Robust waterborne superhydrophobic coatings with reinforced composite interfaces. *ACS Appl. Mater. Interfaces* **12**, 48216–48224 (2020).

66. Verho, T. et al. Reversible switching between superhydrophobic states on a hierarchically structured surface. *Proc. Natl Acad. Sci. USA* **109**, 10210–10213 (2012).

67. Meng, Y. et al. Holistic anti/dewetting design of anti/deicing superhydrophobic surfaces (ADISS). *ACS Mater. Lett.* **6**, 1457–1466 (2024).

68. Xuan, S. et al. Trifolium repens L.-Like periodic micronano struc-tured superhydrophobic surface with ultralow ice adhesion for efficient anti-icing/deicing. *ACS Nano* **17**, 21749–21760 (2023).

69. Liu, D. et al. Superhydrophobic antifrosting 7075 aluminum alloy surface with stable Cassie-Baxter state fabricated through direct laser interference lithography and hydrothermal treatment. *Lang-muir* **40**, 950–959 (2023).

70. Li, L. & Zhang, J. Highly salt-resistant and all-weather solar-driven interfacial evaporators with photothermal and electrothermal effects based on Janus graphene@silicone sponges. *Nano Energy* **81**, 105682 (2021).

71. Huang, D., Wang, W., Xu, J. & Wang, A. Mechanical and water resistance properties of chitosan/poly(vinyl alcohol) films rein-forced with attapulgite dispersed by high-pressure homogeniza-tion. *Chem. Eng. J.* **210**, 166–172 (2012).

72. Zhang, H. et al. Solar anti-icing surface with enhanced condensate self-removing at extreme environmental conditions. *Proc. Natl Acad. Sci. USA* **118**, e2100978118 (2021).

Acknowledgements

Author contributions

Conceptualization: M.Y.M., J.F.W., J.P.Z. Methodology: M.Y.M., J.F.W., B.C.L. Data Analysis: M.Y.M., J.F.W., B.C.L., L.X.L. Investigation: M.Y.M., J.F.W. Supervision: J.P.Z. Writing-original draft: M.Y.M., J.F.W., X.P.H., J.P.Z. Writing-review and editing: M.Y.M., J.F.W., J.P.Z.

Competing interests

The authors declare no competing interests.

Additional information